Research Article

A New Stress Field Model for Semiclosed Crack under Compression considering the Influence of T-Stress

Mingyu Feng ⓘ,[1] **Xiaoguang Zhou ⓘ,**[2] **Yanbin Zhang ⓘ,**[1] **and Saifeng Wu**[3]

[1]*School of Civil Engineering, Beijing Jiaotong University, Key Laboratory of Urban Underground Engineering of Ministry of Education, Beijing 100044, China*
[2]*Department of Ocean Science and Engineering, Southern University of Science and Technology, Shenzhen 518055, China*
[3]*School of Mechanics and Engineering Science, Shanghai University, Shanghai 200444, China*

Correspondence should be addressed to Mingyu Feng; fengmingyu@bjtu.edu.cn

Compression is a typical stress condition for cracks in deep-water structures, where the cracks tend to close from a nonclosed state, due to a certain gap that exists between the surfaces on both sides of cracks. The stress field models around the crack have been established in previous studies, while the crack surfaces are simply assumed in a nonclosed or full-closed state. In fact, the cracks inside deep-water structures are usually in a semiclosed state, leaving the reliability of calculation results in risk. To reflect the actual state of crack, a comprehensive stress field model around the semiclosed crack is established based on the complex potential theory, and the stress intensity factor K_{II} at the crack tip related to the closure amount of crack surfaces, deep-water pressure, friction coefficient in the closed region, and crack inclination angle is derived. The analytical solution of the stress field around the semiclosed crack contains three T-stress components, i.e., T_x, T_y, and T_{xy}. The rationality and effectiveness of the proposed stress field model are verified by the isochromatic fringe patterns around the crack obtained from the photoelastic experiment. It reveals that the proposed model can reasonably predict the evolution of the stress field with the closure amount of crack under constant and variable stress conditions.

1. Introduction

In general, the most common construction material that has been used for off-shore oil production platforms is steel [1–3]; however, more than 50 reinforced concrete platform bases have been utilized by the Norwegians and British in the North Sea [4]. As shown in Figure 1, the reinforced concrete oil platform typically consists of a large gravity base and several concrete legs supporting the upper steel structure. The foundations of offshore wind turbine can also be made of concrete materials [5], as demonstrated in Figure 2. These are massive structures due to the deep-water pressures involved and the wave loading that has to be resisted. However, during the manufacture and construction of these concrete structures, discontinuity defects similar to fault or microcrack are inevitably generated owing to the uneven distribution of early thermal stress

or shrinkage of cementitious materials [6, 7]. Generally, these defects tend to occur and appear in the form of cracks, which can be seen in Figures 1 and 2. It would be no exaggeration to state that cracks have their great influences on the mechanical performance of concrete structure. Crack tips under load are susceptible to stress concentration effects, which in turn cause a reduction in structural capacity significantly through initiation, propagation, and interconnection; on the other hand, the presence of cracks leads to the corrosion of internal reinforcement by reducing the durability of the concrete and further weakens the capacity of the structure, often resulting in serious and disastrous consequences [8].

To realistically evaluate the effect of internal cracks on the structural capacity under deep-water pressure conditions, it is essential to have a clear understanding of the stress field around the cracks. Most previous studies on
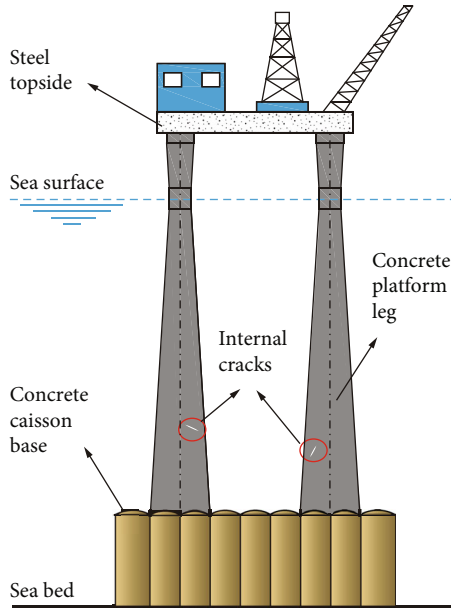
FIGURE 1: The oil platform with concrete legs and concrete base installed on the seabed.
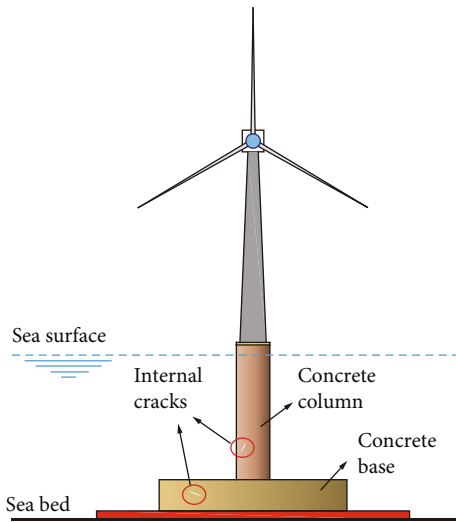
FIGURE 2: Schematic of a gravity-based offshore wind turbine.

crack fracture behavior have focused on the stress field and crack initiation of tension cracks (mode I), and theoretical research on this type crack has become mature [9, 10]. However, the internal cracks in deep-water structures are hardly subjected to such stress states similar to the pure mode I cracks. In fact, these cracks under the action of deep-water pressure, self-weight, and upper load are usually under multiaxial compression stress state, and the surfaces on both sides of the crack cause an interaction due to the closure, including mutual compression and friction effects [11, 12]. Different closure amounts may cause to interact differently between the two surfaces, and these differences may be important to the stress field depending on the magnitude of the influence.

For the analysis of crack problems, the stress field proposed by Williams [13] can well describe the stress distribution near the crack tip. The Williams expression contains not only the singular stress term with $r^{1/2}$ but also the nonsingular stress terms (generally called T-stress) and higher order terms with $O(r^{1/2})$. In the past, only the singular stress term in the expansion is adopted by scholars when studying the stress field at the crack tip [14, 15], ignoring the nonsingular term and the higher-order term. However, numerous studies [16–18] have shown that T-stress has a significant effect on the tip stress field, which can be summarized as follows: when r approaches to 0, the singular stress term in the expansion plays the main controlling role, and as the r gradually increases, the value of the singular stress term decreases rapidly while the proportion of nonsingular stress term gradually increases. It reveals that the nonsingular stress term cannot be ignored in particular under this condition. The study of the stress field near the crack when considering the T-stress under tensile conditions has a relatively mature theoretical basis, but the effects of T-stress in a compressive stress state are rarely considered for studying the stress field around the crack [19, 20].

Many scholars have studied the influence of defects such as inclusions and cracks on the fracture behavior of materials by using experimental and numerical analysis, and Fan et al. [21] conducted uniaxial compression tests on the cuboidal sandstone containing a nonpenetrating crack to study the cracking mechanism of defects. The results show that crack first initiates at the tip of the crack on the front surface of the specimen, while the new crack initiates at the middle of the crack on the back surface. Zhang et al. [22] quantitatively studied the influence of two conditions, with and without inclusions, on the mechanical mechanisms of rock crack evolution, and the impact of inclusions on the mechanical properties of the rock during compressive loading was researched as well. Through a combination of experiments and numerical simulations, Yang et al. [23] investigated the relationship between wing crack expansion and peak strength for specimens containing main crack and prefabricated wing cracks, where it was concluded that the length of the prefabricated wing crack had a negligible effect on the peak strength of the specimen. For the study of crack in the closed state, Liu [24] established the stress field expression around the crack that is full-closed under uniaxial compression; Fan et al. [25] and Feng et al. [26] studied the initiation behavior and the evolution of tangential stress for rock material under compression. Nevertheless, all of the above studies are based on an ideal model with the cracks being in a full-closed state. It is worth noting that a certain gap usually exists between the crack surfaces, and under the action of compression, the crack is actually always in such a practical state; that is, the crack surfaces are gradually closed from the nonclosed state.

To reflect the actual state of cracks in view of the shortcomings of the previous research results, this paper firstly derives a more comprehensive and detailed stress field model containing T-stress around the crack under compression stress state based on the complex potential theory of Muskhelishvili [27], considering not only the mutual

compression and frictional effects between the surfaces on both sides of the crack but also the closure amount of crack surfaces. The rationality of the stress field model is then verified by comparing the isochromatic fringe pattern obtained from the previous photoelastic experiments with the contour lines predicted by the proposed model in this study. Finally, the evolution of stress fields with closure amount under equal stress and variable stress conditions is analyzed and compared, respectively. The aim of this paper is to accurately describe the stress fields of semiclosed cracks; furthermore, the results can also intend to provide a theoretical guidance for accurate and quantitative analysis of the distribution of stress fields around internal cracks in deep-water structures, so as to provide a design reference for structures.

2. Stress Fields of Nonclosed and Full-Closed Crack under Compression

Crack propagation strongly depends on the asymptotic stress field near the crack tip. It is well known that the asymptotic stress field at the crack tip in a two-dimensional elastic medium can be described by the leading singular and secondary constant terms as follows [28]:

$$
\begin{Bmatrix} \sigma_x \\ \sigma_y \\ \tau_{xy} \end{Bmatrix} = \frac{K_I}{\sqrt{2\pi r}} \cos\frac{\theta}{2} \begin{Bmatrix} 1 - \sin\frac{\theta}{2}\sin\frac{3\theta}{2} \\ 1 + \sin\frac{\theta}{2}\sin\frac{3\theta}{2} \\ \sin\frac{\theta}{2}\sin\frac{3\theta}{2} \end{Bmatrix}
$$
$$
+ \frac{K_{II}}{\sqrt{2\pi r}} \begin{Bmatrix} -\sin\frac{\theta}{2}\left(2 + \cos\frac{\theta}{2}\cos\frac{3\theta}{2}\right) \\ \sin\frac{\theta}{2}\cos\frac{\theta}{2}\cos\frac{3\theta}{2} \\ \cos\frac{\theta}{2}\left(1 - \sin\frac{\theta}{2}\sin\frac{3\theta}{2}\right) \end{Bmatrix} \tag{1}
$$
$$
+ \begin{Bmatrix} T_x \\ 0 \\ 0 \end{Bmatrix} + O(r^{1/2}),
$$

where K_I and K_{II} represent the modes I and II stress intensity factors, respectively, which characterize the singular behaviors caused by the normal and shear components of the stress on the crack surfaces. It is worth noting that the asymptotic stress field of Equation (1) is only applicable to open cracks. That is, the application of the crack tip stress field actually requires $K_I \geq 0$, and the above expression no longer holds if $K_I < 0$. It is attributed to the fact that the two crack surfaces are in contact with each other when the crack is closed by compression, and the singular behavior relative to K_I no longer occurs [11, 12]. For the inclined crack with tips in the material, such a trend is always presented at the tip in the process of gradual compression; that
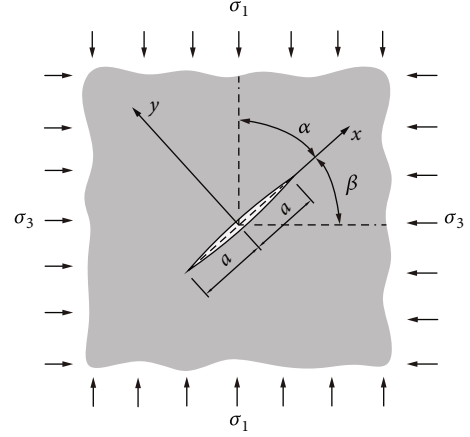
FIGURE 3: Nonclosed crack subjected to compression.

is, the crack transforms from completely nonclosed state to semiclosed state and then to full-closed state. For a nonclosed crack with no interaction between the two sides, as shown in Figure 3, the stress field has been derived by previous scholars [29, 30], which can be expressed as follows:

$$
\begin{Bmatrix} \sigma_x \\ \sigma_y \\ \tau_{xy} \end{Bmatrix} = \frac{K_{II}}{\sqrt{2\pi r}} \begin{Bmatrix} -\sin\frac{\theta}{2}\left(2 + \cos\frac{\theta}{2}\cos\frac{3\theta}{2}\right) \\ \sin\frac{\theta}{2}\cos\frac{\theta}{2}\cos\frac{3\theta}{2} \\ \cos\frac{\theta}{2}\left(1 - \sin\frac{\theta}{2}\sin\frac{3\theta}{2}\right) \end{Bmatrix}
$$
$$
+ \begin{Bmatrix} T_x \\ 0 \\ 0 \end{Bmatrix} + O(r^{1/2}). \tag{2}
$$

Meanwhile, for a full-closed crack with interactions (both compressive stress and friction) on all surfaces, as shown in Figure 4; the analytical solution of the stress field has also been established under this condition [24–26], which can be expressed as follows:

$$
\begin{Bmatrix} \sigma_x \\ \sigma_y \\ \tau_{xy} \end{Bmatrix} = \frac{K_{II}}{\sqrt{2\pi r}} \begin{Bmatrix} -\sin\frac{\theta}{2}\left(2 + \cos\frac{\theta}{2}\cos\frac{3\theta}{2}\right) \\ \sin\frac{\theta}{2}\cos\frac{\theta}{2}\cos\frac{3\theta}{2} \\ \cos\frac{\theta}{2}\left(1 - \sin\frac{\theta}{2}\sin\frac{3\theta}{2}\right) \end{Bmatrix}
$$
$$
+ \begin{Bmatrix} T_x \\ T_y \\ T_{xy} \end{Bmatrix} + O(r^{1/2}). \tag{3}
$$

However, the establishment of the above two stress fields is only based on the ideal condition; that is, the crack is

FIGURE 4: Full-closed crack subjected to compression.

FIGURE 5: Semiclosed crack subjected to compression.

FIGURE 6: The stress mode of the closed region at the crack tip.

under nonclosed or full-closed states. However, the actual situation is that the crack tips gradually close as compression proceeds. Furthermore, the above models are only applicable to the stress field in the very small area of the tip, and the reliability cannot be guaranteed for predicting stress field at distances far from the tip. Therefore, given the actual state of the general crack, it needs to be stated that the stress fields expressed by Equations (2) and (3) still have great limitations in application, and the influence of semiclosed crack on the stress field must be properly understood for their use in concrete fracture mechanics.

3. Stress Fields of Semiclosed Crack under Compression

3.1. Boundary Conditions and Model Assumptions. Consider an elastic infinite plate containing a semiclosed crack of length $2a$ subjected to two vertical stresses σ_1 and σ_3 at infinity, as shown in Figure 5. The angle between the crack and the vertical stress σ_1 is α, and the angle between the crack and the horizontal stress σ_3 is β. The crack tends to close under the action of compression, as illustrated in Figure 6. The two surfaces above and below the closed region of the crack tip produce mutual compression and friction, where the closed length and nonclosed length are denoted by Δa and b, respectively. The expression $\Delta a/a$ is defined as the closure amount in this paper. Due to the existence of a very small gap between the two surfaces of the crack, the crack is no longer strictly linear during the process of tip closure. Comparatively, when the gap between crack surfaces is much smaller than the length of the crack, it can be assumed that the crack is still straight. The compressive stress in the closed region is σ_n, which can be expressed as follows by a function:

$$\sigma_n = f(x), \tag{4}$$

where $f(x)$ is a function in relation to x and σ_N and σ_N is the maximum compressive stress on the closed region, which can be taken as

$$f(x)_{\max} = \sigma_N = \left(\frac{\sigma_1 + \sigma_3}{2} + \frac{\sigma_1 - \sigma_3}{2} \cos 2\beta\right). \tag{5}$$

The shear stress on the closed region surface is given by:

$$\tau_s = \frac{\sigma_1 - \sigma_3}{2} \sin 2\beta. \tag{6}$$

Due to the drive of shear stress, frictional resistance τ_f can be generated in the closed region. When the shear stress τ_s is less than the frictional resistance τ_f on the crack surface, the friction can prevent the crack in the closed region from slipping; when the shear stress τ_s is greater than the frictional resistance τ_f on the surface of the crack, the surfaces on both sides of the closed region relatively slid, and the frictional resistance τ_f on the surface of the closed region is

$$\tau_f = \mu\sigma_n = \frac{1}{2}\mu[(\sigma_1 + \sigma_3) + (\sigma_1 - \sigma_3) \cos 2\beta], \tag{7}$$

where μ represents the friction coefficient. Therefore, the condition for relative sliding of the crack surfaces in the closed region is

$$\tau_s > \tau_f, \tag{8}$$

takes the stress form:

$$(\sigma_1 - \sigma_3) \sin 2\beta > \mu[(\sigma_1 - \sigma_3) + (\sigma_1 - \sigma_3) \cos 2\beta]. \tag{9}$$

3.2. Stress Function. According to Muskhelishvili, the complexity of a problem in the plane theory of elasticity can be simplified very significantly by finding $\Phi(z)$ and $\Omega(z)$, which must satisfy the problem boundary conditions [27]. The stress field at the tip of the crack can always be expressed by these two complex functions:

$$\sigma_x + \sigma_y = 4 \operatorname{Re} [\Phi(z)], \tag{10}$$

$$\sigma_y - i\tau_{xy} = \Phi(z) + \Omega(\bar{z}) + (z - \bar{z})\overline{\Phi}'(z), \tag{11}$$

where $z = x + iy$ and $\bar{z} = x - iy$. σ_y^+ and τ_{xy}^+ and σ_y^- and τ_{xy}^- are defined representing the boundary values of the upper and lower surfaces of the crack, respectively. For the crack shown in Figure 6, the boundary values of surfaces in the closed region can be taken as below.
    Upper surface:

$$\sigma_y^+ = \sigma_n, \tau_{xy}^+ = \tau_f \,;\, \text{for} - a \leq x \leq -b \text{ and } b \leq x \leq a, \tag{12}$$

$$\sigma_y^+ = 0, \tau_{xy}^+ = 0 \,;\, \text{for} - b < x < b. \tag{13}$$

Lower surface:

$$\sigma_y^- = \sigma_n, \tau_{xy}^- = \tau_f \,;\, \text{for} - a \leq x \leq -b \text{ and } b \leq x \leq a, \tag{14}$$

$$\sigma_y^- = 0 \,;\, \tau_{xy}^- = 0 \,;\, \text{for} - b < x < b. \tag{15}$$

By the Equations (11), (12), and (14), the boundary conditions of surfaces in the closed region take the form:

$$\Phi^+(t) + \Omega^-(t) = \sigma_y^+ - i\tau_{xy}^+, \tag{16}$$

$$\Phi^-(t) + \Omega^+(t) = \sigma_y^- - i\tau_{xy}^-, \tag{17}$$

adding and subtracting, which can be obtained:

$$[\Phi(t) + \Omega(t)]^+ + [\Phi(t) + \Omega(t)]^- = 2P(t), \tag{18}$$

$$[\Phi(t) - \Omega(t)]^+ - [\Phi(t) - \Omega(t)]^- = 2Q(t), \tag{19}$$

where $P(t)$ and $Q(t)$ are known functions on the surface in the closed region. The Equations (18) and (19) are typical Riemann-Hilbert problem, which generally takes the following form:

$$F^+(t) = gF^-(t) + f, \tag{20}$$

assume $F(t) = \Phi(t) + \Omega(t)$, the Equation (18) can be obtained when $g = -1$ and $f = 2(\sigma_n - i\tau_f)$; assume $F(t) = \Phi(t) - \Omega(t)$, the Equation (19) can be obtained when $g = 1$ and $f = 0$. The two general solutions to the problem can be obtained, respectively:

$$\Phi(z) + \Omega(z) = \frac{1}{\pi i X(z)} \left[\int_{-a}^{-b} \frac{X(t)P(t)\mathrm{d}t}{t - z} + \int_{b}^{a} \frac{X(t)P(t)\mathrm{d}t}{t - z} \right] + \frac{2P(z)}{X(z)}, \tag{21}$$

$$\Phi(z) - \Omega(z) = \frac{1}{\pi i} \left[\int_{-a}^{-b} \frac{X(t)P(t)\mathrm{d}t}{t - z} + \int_{b}^{a} \frac{X(t)P(t)\mathrm{d}t}{t - z} \right] - \overline{\Gamma}'. \tag{22}$$

The two stress functions can be solved:

$$\Phi(z) = \frac{1}{2\pi i X(z)} \left[\int_{-a}^{-b} \frac{X(t)P(t)\mathrm{d}t}{t - z} + \int_{b}^{a} \frac{X(t)P(t)\mathrm{d}t}{t - z} \right] + \frac{P(z)}{X(z)} - \frac{1}{2}\overline{\Gamma}', \tag{23}$$

$$\Omega(z) = \frac{1}{2\pi i X(z)} \left[\int_{-a}^{-b} \frac{X(t)P(t)\mathrm{d}t}{t - z} + \int_{b}^{a} \frac{X(t)P(t)\mathrm{d}t}{t - z} \right] + \frac{P(z)}{X(z)} + \frac{1}{2}\overline{\Gamma}', \tag{24}$$

where $X(z) = \sqrt{z^2 - a^2}$ and $P(z) = C_0 z$ and the two stress functions can be rewritten as

$$\Phi(z) = \frac{1}{2\pi i \sqrt{z^2 - a^2}} \left[\int_{-a}^{-b} \frac{\sqrt{t^2 - a^2}P(t)}{t - z} \mathrm{d}t + \int_{b}^{a} \frac{\sqrt{t^2 - a^2}P(t)}{t - z} \mathrm{d}t \right] + \frac{C_0 z}{\sqrt{z^2 - a^2}} - \frac{1}{2}\overline{\Gamma}', \tag{25}$$

$$\Omega(z) = \frac{1}{2\pi i \sqrt{z^2 - a^2}} \left[\int_{-a}^{-b} \frac{\sqrt{t^2 - a^2}P(t)}{t - z} \mathrm{d}t + \int_{b}^{a} \frac{\sqrt{t^2 - a^2}P(t)}{t - z} \mathrm{d}t \right] + \frac{C_0 z}{\sqrt{z^2 - a^2}} + \frac{1}{2}\overline{\Gamma}', \tag{26}$$

in which

$$C_0 = \Gamma + \frac{1}{2}\overline{\Gamma}' = -\frac{1}{4}(\sigma_1 + \sigma_3) - \frac{1}{4}(\sigma_1 + \sigma_3)(\cos 2\beta - i \sin 2\beta). \tag{27}$$

It is assumed that the closed crack surface in the closed region is subjected to a uniformly distributed compressive stress as shown in Figure 7; by the Equations (4) and (5), we have

$$f(x) = \sigma_N. \tag{28}$$

The boundary values can be taken as

$$\sigma_n = \sigma_N, \text{for} - a \leq x \leq -b \text{ and } b \leq x \leq a, \tag{29}$$

$$\tau_f = \mu\sigma_n = \mu\sigma_N, \text{for} - a \leq x \leq -b \text{ and } b \leq x \leq a. \tag{30}$$

The $P(t)$ in the stress function is as follows:

$$P(t) = \sigma_n - i\tau_f = \sigma_N(1 - i\mu). \tag{31}$$
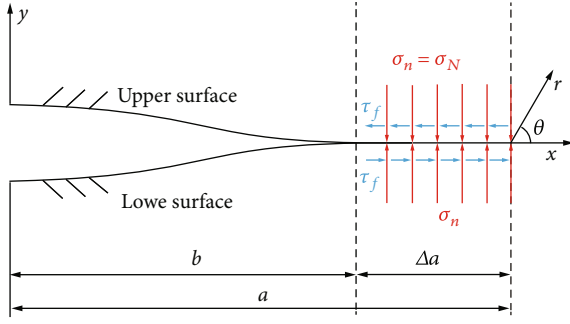
FIGURE 7: The surfaces in closed region subjected to the uniformly distributed compressive stress.

FIGURE 8: The relationship curve between the parameters W and b.

The general expressions of the two stress functions can be obtained:

$$
\begin{aligned}
\Phi(z) = {} & \frac{\sigma_N(1-i\mu)}{2\pi} \left[\pi + \tan^{-1} \frac{-bz-a^2}{\sqrt{a^2-b^2}\sqrt{z^2-a^2}} \right. \\
& \left. - \tan^{-1} \frac{bz-a^2}{\sqrt{a^2-b^2}\sqrt{z^2-a^2}} \right] - \frac{\sigma_N(1-i\mu)z}{\pi\sqrt{z^2-a^2}} \\
& \cdot \left(\frac{\pi}{2} - \sin^{-1}\frac{b}{a} \right) + \frac{C_0 z}{\sqrt{z^2-a^2}} - \frac{1}{2}\overline{\Gamma}',
\end{aligned}
\tag{32}
$$

$$
\begin{aligned}
\Omega(z) = {} & \frac{\sigma_N(1-i\mu)}{2\pi} \left[\pi + \tan^{-1} \frac{-bz-a^2}{\sqrt{a^2-b^2}\sqrt{z^2-a^2}} \right. \\
& \left. - \tan^{-1} \frac{bz-a^2}{\sqrt{a^2-b^2}\sqrt{z^2-a^2}} \right] - \frac{\sigma_N(1-i\mu)z}{\pi\sqrt{z^2-a^2}} \\
& \cdot \left(\frac{\pi}{2} - \sin^{-1}\frac{b}{a} \right) + \frac{C_0 z}{\sqrt{z^2-a^2}} + \frac{1}{2}\overline{\Gamma}'.
\end{aligned}
\tag{33}
$$

3.3. Stress Intensity Factor.

The relationship between the stress intensity factors K_I and K_{II} for mode I and mode II of inclined crack in the infinite plane can be expressed as [19, 31]

$$
K_I - iK_{II} = \lim_{z \longrightarrow a} 2\sqrt{2\pi(z-a)}\Phi(z),
\tag{34}
$$

the term $\sigma_N(1-i\mu)$ in the stress function is given by

$$
\sigma_N(1-i\mu) = -\frac{1}{2}(1-i\mu)[\sigma_1 + \sigma_3 + (\sigma_1 - \sigma_3)\cos 2\beta].
\tag{35}
$$

Thus, the Equation (34) can then be expressed by

$$
\begin{aligned}
K_I - iK_{II} = {} & -\frac{1}{2}\sqrt{\pi a}\{(\sigma_1+\sigma_3) + (\sigma_1+\sigma_3)\cos 2\beta \\
& - 2[\sigma_1+\sigma_3+(\sigma_1-\sigma_3)\cos 2\beta]W\} \\
& - \frac{1}{2}i\sqrt{\pi a}\{(\sigma_1+\sigma_3)\sin 2\beta \\
& - 2\mu[\sigma_1+\sigma_3+(\sigma_1-\sigma_3)\cos 2\beta]W\},
\end{aligned}
\tag{36}
$$

where

$$
W = \frac{1}{\pi}\left(\frac{\pi}{2} - \sin^{-1}\frac{b}{a} \right).
\tag{37}
$$

From Equation (36) the stress intensity factors K_I and K_{II} ahead of the crack tip are separately expressed as

$$
K_I = -\frac{1}{2}\sqrt{\pi a}[\sigma_1+\sigma_3+(\sigma_1-\sigma_3)\cos 2\beta](1-2W),
\tag{38}
$$

$$
\begin{aligned}
K_{II} = {} & \frac{1}{2}\sqrt{\pi a}\{(\sigma_1-\sigma_3)\sin 2\beta \\
& - 2\mu[\sigma_1+\sigma_3+(\sigma_1-\sigma_3)\cos 2\beta]W\}.
\end{aligned}
\tag{39}
$$

Figure 8 shows the relationship curve between the parameters W and b; it can be seen that W takes the range of values $0.5 \geq W \geq 0$ when b takes a range of values $0 \leq b \leq a$, and the term $(1-2W)$ in Equation (38) falls between the range of 0 to 1, indicating that the mode I stress intensity factor K_I at the crack tip is a nonpositive value under compression. In addition, due to the noninvasive nature of the material, it can be considered that the crack tip does not have the characteristics of a mode I under the compression condition, that is $K_I = 0$.

Furthermore, when $b = 0$, $W = 0.5$, and $K_I = 0$ it reveal that the crack surface is full-closed and the singular term in relation to the mode I crack disappears, which is consistent with previous research results [24–26]. For this case, the expression for K_{II} is given by

$$
\begin{aligned}
K_{II} = {} & \frac{1}{2}\sqrt{\pi a}\{(\sigma_1-\sigma_3)\sin 2\beta \\
& - \mu[\sigma_1+\sigma_3+(\sigma_1-\sigma_3)\cos 2\beta]\}.
\end{aligned}
\tag{40}
$$

The above equation is the same as the stress intensity factor for the full-closed crack tip obtained by Fan et al. [25]. For the case when $b = a$ and $W = 0$, the crack surfaces
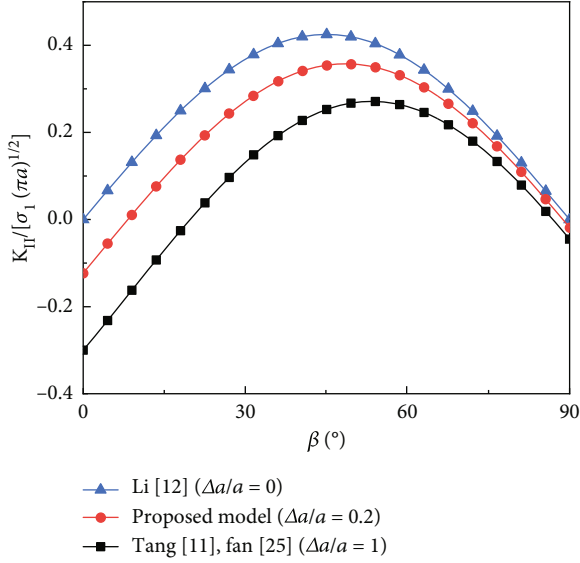
FIGURE 9: Comparison of the variation of normalized stress intensity factor as a function of crack inclination angle obtained from the proposed and the previous theories.
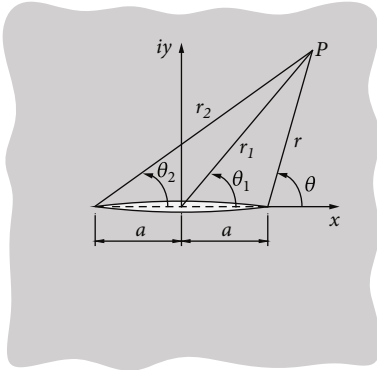
FIGURE 10: The coordinate system of the crack.

are closed but without interaction, and the stress intensity factor is

$$K_{II} = \frac{1}{2}\sqrt{\pi a}(\sigma_1 - \sigma_3)\sin 2\beta. \tag{41}$$

Figure 9 shows the comparison of the variation of normalized stress intensity factor as a function of crack inclination angle obtained from the proposed theory and the previous theories [11, 12, 25]. As we can see, for the three models, the stress intensity factor has the characteristic of decreasing with the increase of the crack inclination angle. Besides, the stress intensity factor obtained from the semiclosed model in this paper is in between that of the nonclosed model and the full-closed model for the same crack inclination angle, and different crack inclination angles corresponding to the maximum values of the stress intensity factor can be determined from the three different closed models.

For the semiclosed crack, the condition for relative sliding of the crack surfaces is defined by the Equations (8) and
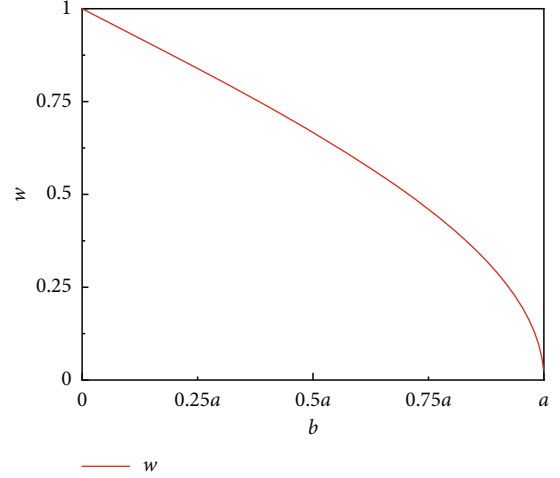
FIGURE 11: The relationship curve between the parameters w and b.

(9), combining with the value range of W in Equation (39), the following equation always set up:

$$(\sigma_1 - \sigma_3)\sin 2\beta - 2\mu[\sigma_1 + \sigma_3 + (\sigma_1 - \sigma_3)\cos 2\beta]W > 0. \tag{42}$$

To sum up, the mode II stress intensity factor K_{II} at the tip of a semiclosed crack is a parameter related to the closure amount, the confining pressure of deep water, the friction coefficient in the closed region, and the inclination angle of crack.

3.4. Analytical Solution of Stress Fields. The analytical solution of stress fields near the crack tip subjected to the loading in Figure 5 can be derived by the two stress function $\Phi(z)$ and $\Omega(z)$. The coordinate system defining a double-ended crack in a complex z-plane is shown in Figure 10. Considering the coordinate origin at the center of the crack, the complex variable z is defined as $z = x + iy$. Thus, the P represents a point in the z-plane where the elastic stresses σ_x, σ_y, and τ_{xy} are determined at (θ_1, r_1). According to the polar coordinate system in which the crack is located, the relevant variables are defined as follows:

$$z = r_1 e^{i\theta_1} \, ; z - a = re^{i\theta} \, ; z + a = r_2 e^{i\theta_2}, \tag{43}$$

$$\sqrt{z^2 - a^2} = \sqrt{(z+a)(z-a)} = \sqrt{r}e^{i\theta/2}\sqrt{r_2}e^{i\theta_2/2}. \tag{44}$$

The stress function is expressed in terms of stress intensity factor as

$$\Phi(z) = \frac{\sigma_N(1 - i\mu)}{2\pi}\left[\pi + \tan^{-1}\frac{-bz - a^2}{\sqrt{a^2 - b^2}\sqrt{z^2 - a^2}}\right.$$
$$\left. - \tan^{-1}\frac{bz - a^2}{\sqrt{a^2 - b^2}\sqrt{z^2 - a^2}}\right] - \frac{izK_{II}}{2\sqrt{\pi a}\sqrt{z^2 - a^2}} - \frac{1}{2}\overline{\Gamma}', \tag{45}$$

$$\Omega(z) = \frac{\sigma_N(1 - i\mu)}{2\pi}\left[\pi + \tan^{-1}\frac{-bz - a^2}{\sqrt{a^2 - b^2}\sqrt{z^2 - a^2}}\right.$$
$$\left. - \tan^{-1}\frac{bz - a^2}{\sqrt{a^2 - b^2}\sqrt{z^2 - a^2}}\right] - \frac{izK_{II}}{2\sqrt{\pi a}\sqrt{z^2 - a^2}} + \frac{1}{2}\overline{\Gamma}'.$$

$$(46)$$

Inserting Equations (43) and (44) into Equations (45) and (46), the expressions of the two stress functions in a polar coordinate system are given by

$$\Phi(z) = -\frac{K_{II}r_1}{2\sqrt{\pi arr_2}}\left[-\sin\left(\theta_1 - \frac{\theta + \theta_2}{2}\right) + i\cos\left(\theta_1 - \frac{\theta + \theta_2}{2}\right)\right]$$
$$+ \frac{\sigma_N(1 - i\mu)}{2\pi}\left[\pi - 2\tan^{-1}\frac{b}{\sqrt{a^2 - b^2}}\right] - \frac{1}{2}\overline{\Gamma}',$$

$$(47)$$

$$\Omega(z) = -\frac{K_{II}r_1}{2\sqrt{\pi arr_2}}\left[-\sin\left(\theta_1 - \frac{\theta + \theta_2}{2}\right)\right.$$
$$\left. + i\cos\left(\theta_1 - \frac{\theta + \theta_2}{2}\right)\right] + \frac{\sigma_N(1 - i\mu)}{2\pi}$$
$$\cdot\left[\pi - 2\tan^{-1}\frac{b}{\sqrt{a^2 - b^2}}\right] + \frac{1}{2}\overline{\Gamma}'.$$

$$(48)$$

Therefore, the other functions $\Phi'(z)$, $\overline{\Phi'(z)}$, and $\Omega(\bar{z})$ in Equation (11) can be rewritten as

$$\Phi'(z) = \frac{a^2 K_{II}}{2\sqrt{\pi a}(rr_2)^{3/2}}\left\{\sin\left[\frac{3}{2}(\theta + \theta_2)\right] + i\cos\left[\frac{3}{2}(\theta + \theta_2)\right]\right\},$$

$$(49)$$

$$\overline{\Phi'(z)} = \frac{a^2 K_{II}}{2\sqrt{\pi a}(rr_2)^{3/2}}\left\{\sin\left[\frac{3}{2}(\theta + \theta_2)\right] - i\cos\left[\frac{3}{2}(\theta + \theta_2)\right]\right\},$$

$$(50)$$

$$\Omega(\bar{z}) = -\frac{K_{II}r_1}{2\sqrt{\pi arr_2}}\left[\sin\left(\theta_1 - \frac{\theta + \theta_2}{2}\right)\right.$$
$$\left. + i\cos\left(\theta_1 - \frac{\theta + \theta_2}{2}\right)\right] + \frac{\sigma_N(1 - i\mu)}{2\pi}$$
$$\cdot\left[\pi - 2\tan^{-1}\frac{b}{\sqrt{a^2 - b^2}}\right] - \frac{1}{2}\overline{\Gamma}'.$$

$$(51)$$

By the Equation (10), the relationship between the stress components σ_x and σ_y of the stress field around the crack can be written as follows:

$$\sigma_x + \sigma_y = 4\operatorname{Re}\left[\Phi(z)\right] = \frac{2K_{II}r_1}{\sqrt{\pi arr_2}}\sin\left(\theta_1 - \frac{\theta + \theta_2}{2}\right)$$
$$+ (\sigma_1 - \sigma_3)\cos 2\beta - [\sigma_1 + \sigma_3 + (\sigma_1 - \sigma_3)\cos 2\beta]$$
$$\cdot\frac{1}{\pi}\left[\pi - 2\tan^{-1}\frac{b}{\sqrt{a^2 - b^2}}\right].$$

$$(52)$$

Similarly, apply the proper functions given above to Equation (11) to get the relationship between the stress components σ_y and τ_{xy}:

$$\sigma_y - i\tau_{xy} = \Phi(z) + \Omega(\bar{z}) + (z - \bar{z})\overline{\Phi}'(z)$$
$$= -\frac{K_{II}r_1}{2\sqrt{\pi arr_2}}\left[-\sin\left(\theta_1 - \frac{\theta + \theta_2}{2}\right)\right.$$
$$\left. + i\cos\left(\theta_1 - \frac{\theta + \theta_2}{2}\right)\right] + \frac{\sigma_N(1 - i\mu)}{\pi}$$
$$\cdot\left[\pi - 2\tan^{-1}\frac{b}{\sqrt{a^2 - b^2}}\right] - \frac{K_{II}r_1}{2\sqrt{\pi arr_2}}$$
$$\cdot\left[\sin\left(\theta_1 - \frac{\theta + \theta_2}{2}\right) + i\cos\left(\theta_1 - \frac{\theta + \theta_2}{2}\right)\right]$$
$$+ \frac{2ira^2 K_{II}}{\sqrt{\pi a}(rr_2)^{3/2}}\sin\frac{\theta}{2}\cos\frac{\theta}{2}$$
$$\cdot\left\{\sin\left[\frac{3}{2}(\theta + \theta_2)\right] - i\cos\left[\frac{3}{2}(\theta + \theta_2)\right]\right\}.$$

$$(53)$$

Extracting the real and imaginary parts of Equation (53), the stress components σ_y and τ_{xy} can be obtained:

$$\sigma_y = \frac{2ra^2 K_{II}}{\sqrt{\pi a}(rr_2)^{3/2}}\sin\frac{\theta}{2}\cos\frac{\theta}{2}\cos\frac{3}{2}(\theta + \theta_2)$$
$$- \frac{1}{2}[\sigma_1 + \sigma_3 + (\sigma_1 - \sigma_3)\cos 2\beta]\frac{1}{\pi}$$
$$\cdot\left[\pi - 2\tan^{-1}\frac{b}{\sqrt{a^2 - b^2}}\right].$$

$$(54)$$

$$\tau_{xy} = \frac{K_{II}r_1}{\sqrt{\pi arr_2}}\cos\left(\theta_1 - \frac{\theta + \theta_2}{2}\right)$$
$$- \frac{2ra^2 K_{II}}{\sqrt{\pi a}(rr_2)^{3/2}}\sin\frac{\theta}{2}\cos\frac{\theta}{2}\sin\frac{3}{2}(\theta + \theta_2)$$
$$- \frac{1}{2}\mu[\sigma_1 + \sigma_3 + (\sigma_1 - \sigma_3)\cos 2\beta]\frac{1}{\pi}$$
$$\cdot\left[\pi - 2\tan^{-1}\frac{b}{\sqrt{a^2 - b^2}}\right].$$

$$(55)$$

Combining Equations (52) and (54) yields the stress component σ_x, as follows:

$$\sigma_x = \frac{2K_{II}r_1}{\sqrt{\pi arr_2}}\sin\left(\theta_1 - \frac{\theta + \theta_2}{2}\right)$$
$$- \frac{2ra^2 K_{II}}{\sqrt{\pi a}(rr_2)^{3/2}}\sin\frac{\theta}{2}\cos\frac{\theta}{2}\cos\frac{3}{2}(\theta + \theta_2)$$
$$- \frac{1}{2}[\sigma_1 + \sigma_3 + (\sigma_1 - \sigma_3)\cos 2\beta]\frac{1}{\pi}$$
$$\cdot\left[\pi - 2\tan^{-1}\frac{b}{\sqrt{a^2 - b^2}}\right] + (\sigma_1 - \sigma_3)\cos 2\beta.$$

$$(56)$$

(a)

(b)

(c)
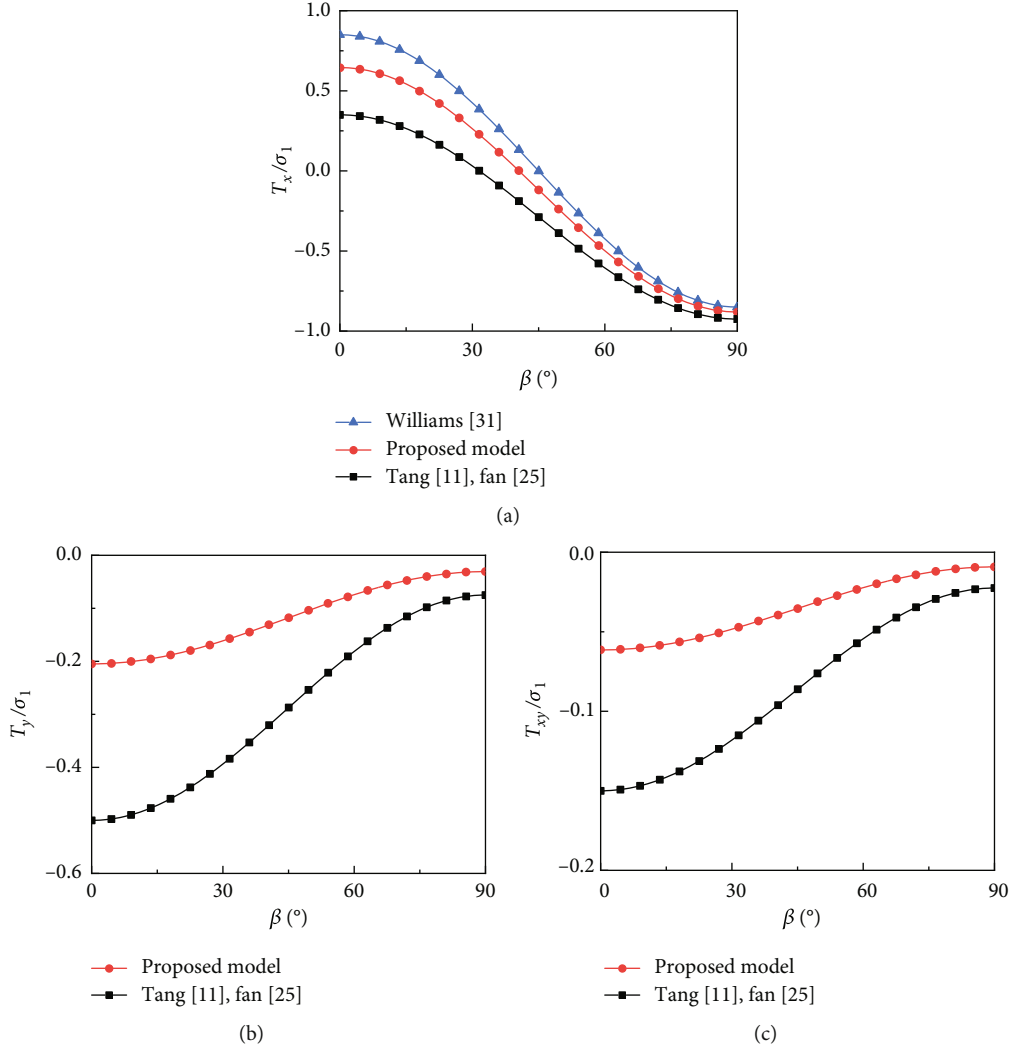
Figure 12: Comparison of the variation of normalized T-stress components as a function of crack inclination angle obtained from the proposed and the previous theories: (a) T_x, (b) T_y, and (c) T_{xy}.
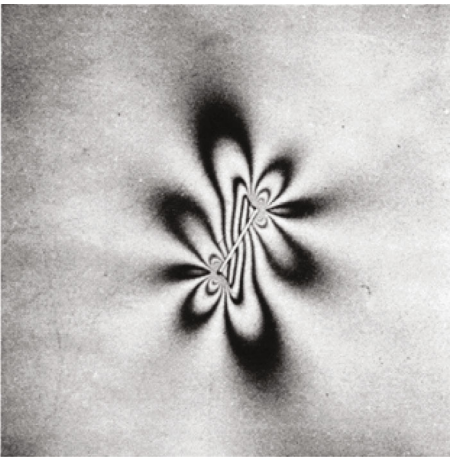
Figure 13: The typical isochromatic pattern around the nonclosed inclined crack in the plate [36].

With respect to Equations (54), (55), and (56), one can see that each stress component contains a subterm related to the stress intensity factor K_{II} and r, and the other subterm is unrelated to K_{II} and r, the latter subterm is the T-stress, which can be expressed by the three T-stress components T_x, T_y, and T_{xy}, respectively:

$$T_x = -\frac{1}{2}[\sigma_1 + \sigma_3 + (\sigma_1 - \sigma_3)\cos 2\beta]w + (\sigma_1 - \sigma_3)\cos 2\beta,$$

(57)

$$T_y = -\frac{1}{2}[\sigma_1 + \sigma_3 + (\sigma_1 - \sigma_3)\cos 2\beta]w,$$

(58)

$$T_{xy} = -\frac{1}{2}\mu[\sigma_1 + \sigma_3 + (\sigma_1 - \sigma_3)\cos 2\beta]w,$$

(59)

where

$$w = \frac{1}{\pi}\left(\pi - 2\tan^{-1}\frac{b}{\sqrt{a^2 - b^2}}\right).$$

(60)

(a) (b) (c)

(d) (e) (f)
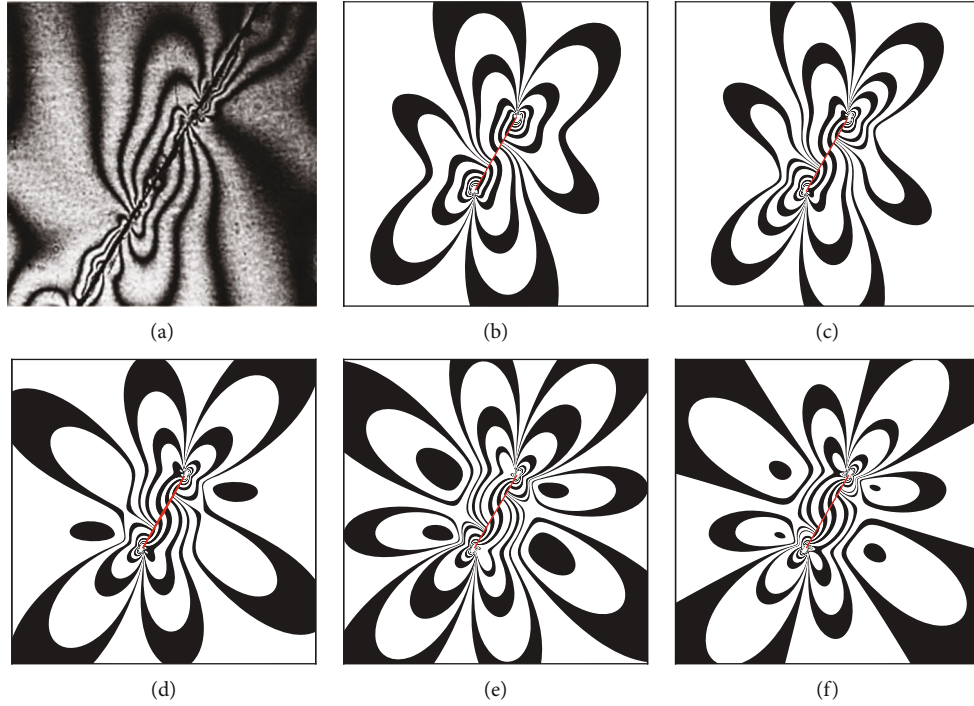
FIGURE 14: The comparison of isochromatic fringe patterns obtained from experiment and model: (a) the results of photoelastic experiment [37]; the results of the proposed model: (b) $\Delta a/a = 0$; (c) $\Delta a/a = 0.25$; (d) $\Delta a/a = 0.5$; (e) $\Delta a/a = 0.75$; and (f) $\Delta a/a = 1$.

Figure 11 illustrates the relationship between the w and b. From the figure one can see that w takes the range of values $1 \geq w \geq 0$ when b takes a range of values $0 \leq b \leq a$. For the specific case that $w \rightarrow 1$ as $b \rightarrow 0$, the three T-stress components are the same as those in full-closed crack obtained by Tang [11] and Fan et al. [25].

Figure 12 compares the variation of the three normalized T-stress components as a function of crack inclination angle obtained from the proposed theory and the previous theories [11, 25, 32]. By comparison, it can be seen that the three stress components obtained from the semiclosed model are larger than those obtained from the full-closed model under the same inclination angle, and the T_x obtained from this paper is smaller than that obtained from the nonclosed model.

In summary, it is clear from Equations (57)–(59) that the T-stress in stress field is the component in relation to the closure amount, confining pressure of deep water, friction coefficient in the closed region, and inclination angle of the crack. So far, the expressions of the three individual stress components σ_x, σ_y, and τ_{xy} in stress field around the semiclosed crack under compression have been already derived as

$$\sigma_x = \frac{2K_{II}r_1}{\sqrt{\pi a}rr_2} \sin\left(\theta_1 - \frac{\theta + \theta_2}{2}\right) \\ - \frac{2ra^2K_{II}}{\sqrt{\pi a}(rr_2)^{3/2}} \sin\frac{\theta}{2}\cos\frac{\theta}{2}\cos\frac{3}{2}(\theta + \theta_2) + T_x, \tag{61}$$

$$\sigma_y = \frac{2ra^2K_{II}}{\sqrt{\pi a}(rr_2)^{3/2}} \sin\frac{\theta}{2}\cos\frac{\theta}{2}\cos\frac{3}{2}(\theta + \theta_2) + T_y, \tag{62}$$

$$\tau_{xy} = \frac{K_{II}r_1}{\sqrt{\pi a}rr_2} \cos\left(\theta_1 - \frac{\theta + \theta_2}{2}\right) \\ - \frac{2ra^2K_{II}}{\sqrt{\pi a}(rr_2)^{3/2}} \sin\frac{\theta}{2}\cos\frac{\theta}{2}\sin\frac{3}{2}(\theta + \theta_2) + T_{xy}. \tag{63}$$

4. Verification of the Stress Field Model

Quantitative visualization gradually becomes an essential experimental tool to understand the stress field evolution which govern mechanical and fracture behaviors in various engineering applications. The photoelastic method enables visualization of the stress field near the crack; therefore, the results of photoelastic fringe pattern have been used to fit the parameters in the analytical solution of the stress field in numerous studies [33–35]. In the photoelastic theory in two-dimensional plane, the difference of principal stresses can be expressed by isochromatic fringe order N, the material fringe value f, and the thickness of the plane h:

$$\sigma_1' - \sigma_2' = \frac{Nf}{h}. \tag{64}$$

For the plane stress problem, the principal stresses can be written as

$$\sigma_1', \sigma_2' = \frac{\sigma_x + \sigma_y}{2} \pm \frac{1}{2}\sqrt{(\sigma_x - \sigma_y)^2 + 4\tau_{xy}^2}. \tag{65}$$

Inserting Equations (61)–(63) into (65) and combining (64), one can obtain the theoretical isochromatic fringes around the crack. It should be noted that the principal

(a)   (b)   (c)
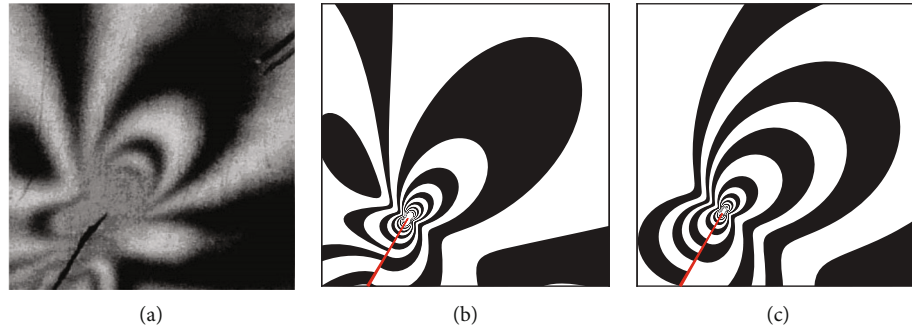
FIGURE 15: The comparison of isochromatic fringe patterns at crack tip obtained from experiment and models: (a) experimental results [38]; (b) the results of proposed model; and (c) the results of Fan's model [25].

(a)   (b)   (c)   (d)
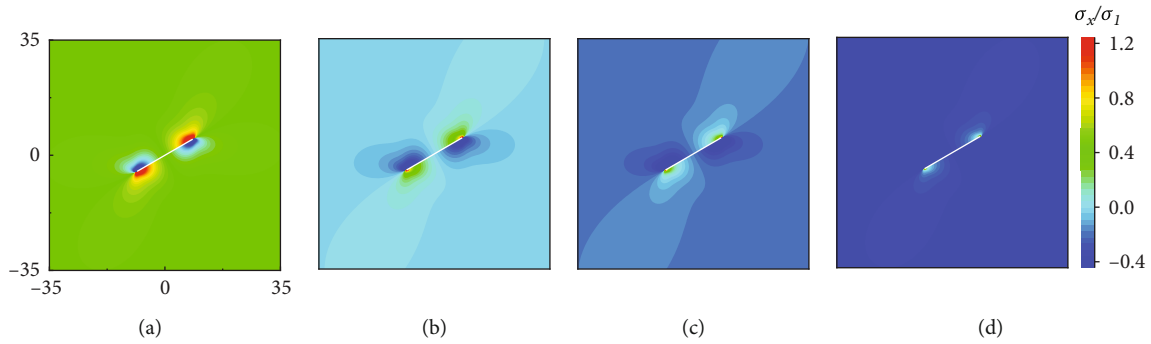
FIGURE 16: The contour plot of normalized σ_x around the crack: (a) $\Delta a/a = 0$; (b) $\Delta a/a = 0.35$; (c) $\Delta a/a = 0.65$; and (d) $\Delta a/a = 1$.

(a)   (b)   (c)   (d)
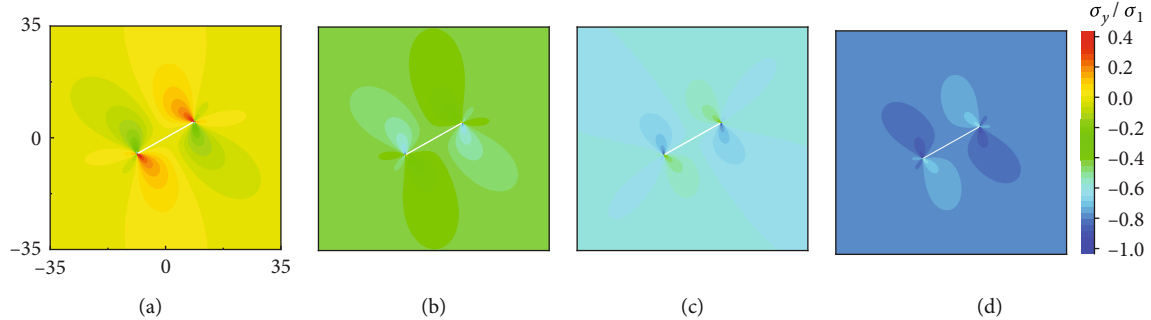
FIGURE 17: The contour plot of normalized σ_y around the crack: (a) $\Delta a/a = 0$; (b) $\Delta a/a = 0.35$; (c) $\Delta a/a = 0.65$; and (d) $\Delta a/a = 1$.

stresses σ_1' and σ_2' herein are different from the far-field stresses σ_1 and σ_2 subjected to the plate containing a crack. Hoek and Bieniawski [36] conducted the photoelastic experiment on glass plate containing a single nonclosed inclined crack under uniaxial compression, a typical isochromatic pattern obtained around the crack in the plate, as illustrated in Figure 13.

Lee et al. [37] studied the evolution of isochromatic fringes around the crack in the Homalite-100 plate under compression and compared the experimental results with the numerical simulation results so as to determine the distribution of stress field. Since it is difficult to achieve a full-closed state on both sides of the crack during the specimen production process at the beginning of compression, we assume that the crack surfaces are in a state of semiclosed. The stress field model proposed in this paper can predict the isochromatic fringes of principal stress difference around the crack under various closure amounts; therefore, the rationality of the proposed model can be verified by comparing the theoretical isochromatic fringes obtained by the model with the isochromatic fringe patterns obtained by the photoelastic experiment. Figure 14 presents the results on the comparison of the isochromatic fringe patterns from photoelastic experiment and theoretical prediction, in which Figure 14(a) shows the distribution of isochromatic fringe patterns around the crack with length of 11 mm and inclination angle of 60° when the axial stress is 36.2 MPa in the uniaxial compression test, and Figures 14(b)–14(f) are the theoretical isochromatic fringes predicted by the proposed model in this paper when the closure amount $\Delta a/a = 0$, 0.25, 0.5, 0.75, and 1, respectively, where the friction coefficient of the crack surface is $\mu = 0.7$.
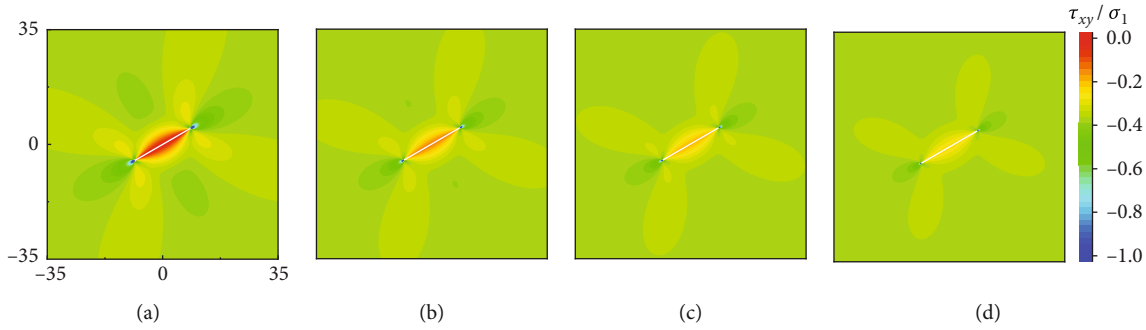
FIGURE 18: The contour plot of normalized τ_{xy} around the crack: (a) $\Delta a/a = 0$; (b) $\Delta a/a = 0.35$; (c) $\Delta a/a = 0.65$; and (d) $\Delta a/a = 1$.
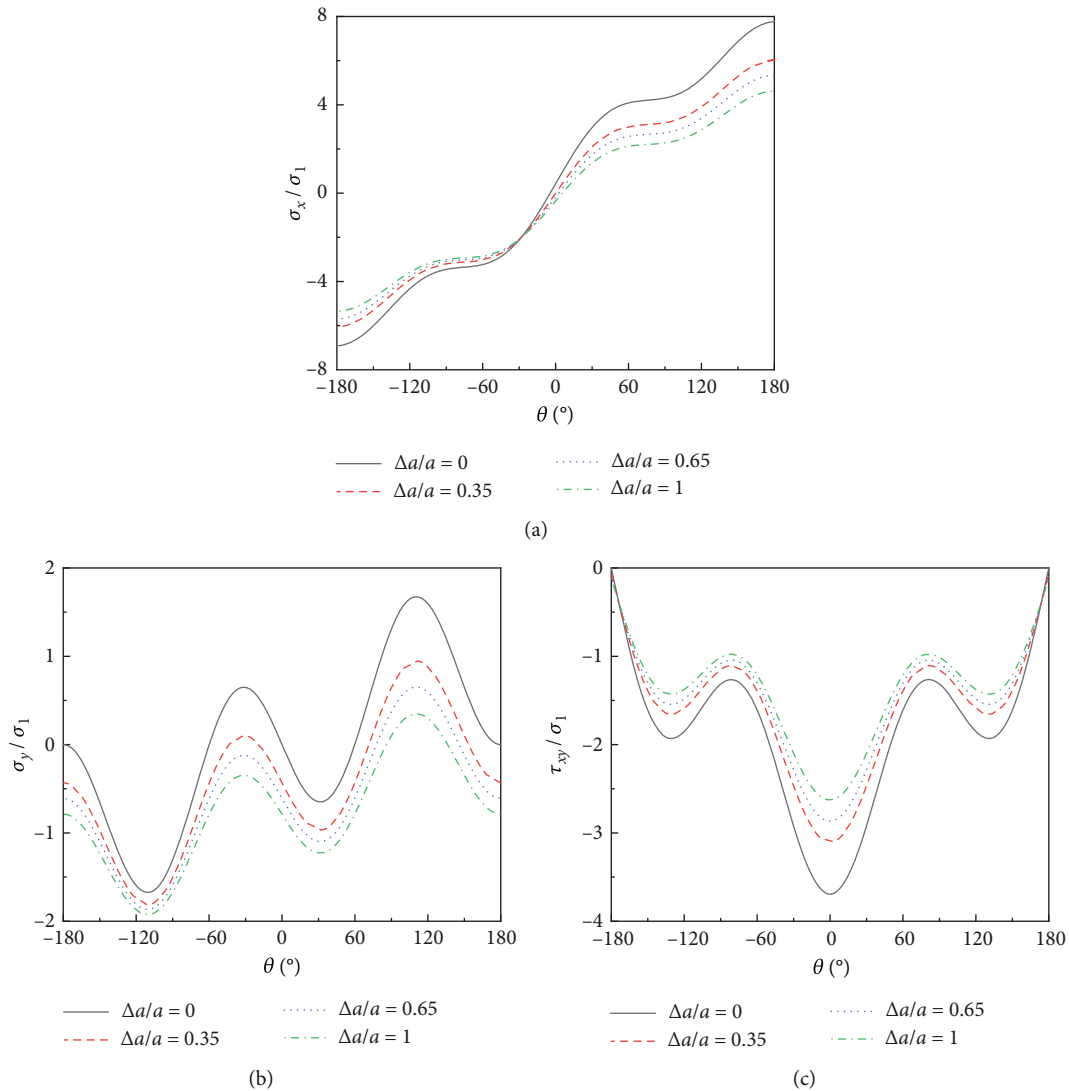
FIGURE 19: Comparison of normalized stress components on a circle with radius of 0.05 mm around the crack tip at different closures: (a) σ_x; (b) σ_y; and (c) τ_{xy}.

The comparison in Figure 14 reveals that when the crack surfaces are nonclosed or full-closed, the discrepancy between theoretical isochromatic fringe patterns and experimental results is considerable, while when the crack surfaces are semiclosed, theoretical results are in better agreements

with the experimental results, especially under the relatively lower closure amount of crack surfaces.

In order to study the effect of crack location and orientation around the tunnel on the stress intensity factor, Wang et al. [38] conducted a series of uniaxial compression tests
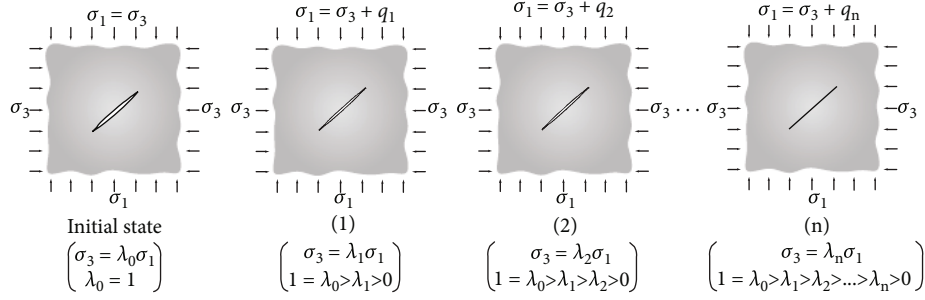
FIGURE 20: Loading path.
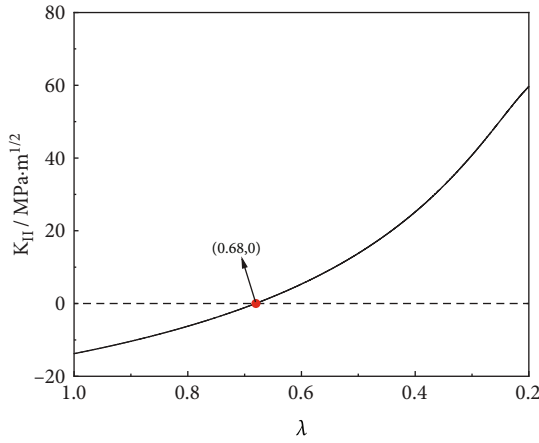
FIGURE 21: The relationship between the stress intensity factor and confining pressure coefficient for $\mu = 0.3$.

on samples made of transparent epoxy resins containing a single crack with different inclination angles and analyzed the photoelastic characteristics of crack near the tip. The distribution of isochromatic fringe patterns, only at the semiclosed crack tip, was investigated to further verify the rationality of the model proposed in this paper. An outcome of a comparison between the experimental results by Wang et al. [38], the model estimation in this paper, and the model estimation obtained by Fan et al. [25] is shown in Figure 15; in the two model estimations, the closure amount and the friction coefficient are taken as 0.2 and 0.3, respectively. It is revealed that there are somewhat differences between the experimental results and the isochromatic fringe patterns predicted by Fan et al. [25] who considered the crack in a full-closed state, while relatively good agreements exist between experimental results and predicted results of the model in this paper.

As may be seen from the above comparisons, the predictions of the proposed semiclosed stress field model are accurate in representing the morphology of isochromatic fringe patterns which represents the stress field distribution on both of the crack and its tips.

5. Evolution of the Stress Field as the Crack Transitions from a Nonclosed to a Full-Closed State

5.1. The Influence of Closure Amount under Constant Stress. It is assumed that internal cracks in deep-water structures

are subjected to constant stress σ_1 caused by self-weight or upper loads and constant stress σ_3 caused by the deep-water pressure, and the particular influence of different closure amount on evolution of stress fields is investigated in this section. The three stress components are normalized dividing both sides of Equations (61) to (63) by σ_1, taking Equation (61) as an example, the equation can be written as

$$\frac{\sigma_x}{\sigma_1} = \frac{2K_{II}r_1}{\sigma_1\sqrt{\pi a r r_2}} \sin\left(\theta_1 - \frac{\theta + \theta_2}{2}\right)$$
$$- \frac{2ra^2 K_{II}}{\sigma_1\sqrt{\pi a}(rr_2)^{3/2}} \sin\frac{\theta}{2} \cos\frac{\theta}{2} \cos\frac{3}{2}(\theta + \theta_2)$$
$$- \frac{1}{2}\left[1 + \lambda + (1 - \lambda)\cos 2\beta\right]\frac{1}{\pi}\left[\pi - 2\tan^{-1}\frac{b}{\sqrt{a^2 - b^2}}\right]$$
$$+ (1 - \lambda)\cos 2\beta,$$

(66)

where

$$\frac{K_{II}}{\sigma_1} = \frac{1}{2}\sqrt{\pi a}\left\{(1 - \lambda)\sin 2\beta - 2\mu[1 + \lambda + (1 - \lambda)\cos 2\beta]\frac{1}{\pi}\left(\frac{\pi}{2} - \sin^{-1}\frac{b}{a}\right)\right\}.$$

(67)

In the Equations (66) and (67), λ represents the water confining pressure coefficient, which can be expressed by $\lambda = \sigma_3/\sigma_1$.

A finite domain with a dimension of $70 \times 70 \, \text{mm}^2$ contains a crack with length of 20 mm, and inclination angle of $30°$ was selected as the studied area. The friction coefficient μ of the crack surfaces in the closed region was taken as 0.3, and the water confining pressure coefficient λ was taken as 0.15. Figures 16–18 show the variation of the contour maps around the crack of the three normalized stress components with the closed amounts, respectively.

From the above figures, it can be concluded that closure amount generally exhibits significant and visible effects on the stress fields around the crack. The crack tip has a more obvious stress concentration effect at lower closure amount in comparison to the higher one. For the stress components σ_x and σ_y under the same boundary conditions, the tensile stress (positive sign) area near the two crack tips gradually
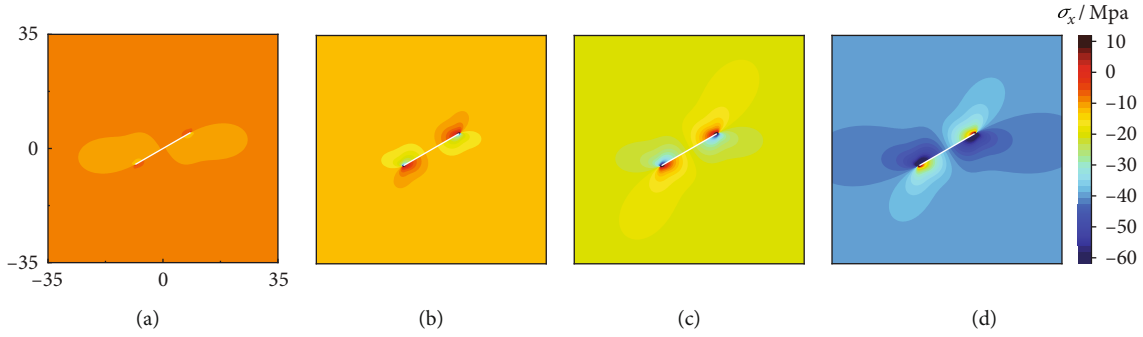
FIGURE 22: The contour plot of σ_x around the crack: (a) $\lambda = 0.6$, $\Delta a/a = 0.33$; (b) $\lambda = 0.4$, $\Delta a/a = 0.50$; (c) $\lambda = 0.3$, $\Delta a/a = 0.67$; and (d) $\lambda = 0.2$, $\Delta a/a = 1$.
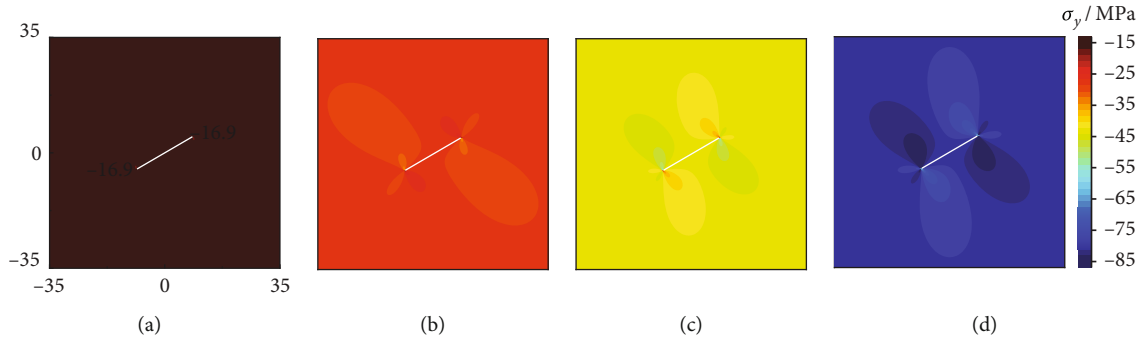
FIGURE 23: The contour plot of σ_y around the crack: (a) $\lambda = 0.6$, $\Delta a/a = 0.33$; (b) $\lambda = 0.4$, $\Delta a/a = 0.50$; (c) $\lambda = 0.3$, $\Delta a/a = 0.67$; and (d) $\lambda = 0.2$, $\Delta a/a = 1$.
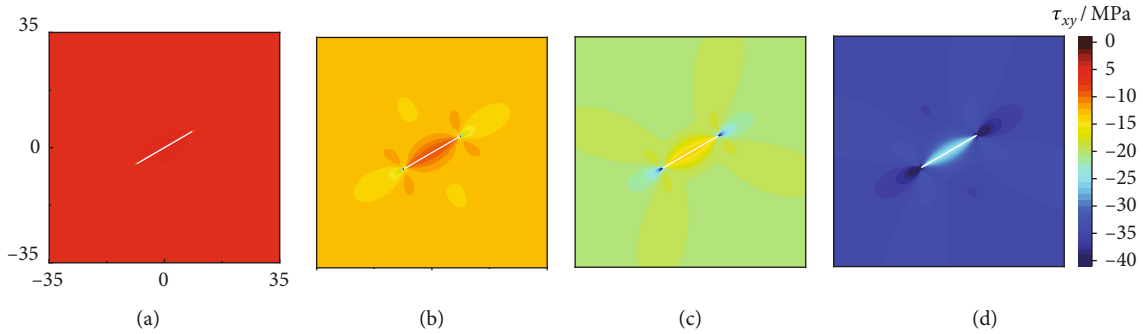
FIGURE 24: The contour plot of τ_{xy} around the crack: (a) $\lambda = 0.6$, $\Delta a/a = 0.33$; (b) $\lambda = 0.4$, $\Delta a/a = 0.50$; (c) $\lambda = 0.3$, $\Delta a/a = 0.67$; and (d) $\lambda = 0.2$, $\Delta a/a = 1$.

decreases with the increase of the closure amount, while the compression stress (negative sign) area gradually increases. It can be clearly seen from Figures 16(d) and 17(d) that the compressive stress area around the crack almost occupies the entire observed area under the condition of $\Delta a/a = 1$. For the stress component τ_{xy}, the whole observed area is a region of compressive stress, it can be observed that the low compressive stress area on both sides of the crack gradually transitions to a relatively higher compressive stress as the closure volume increases; on the contrary, the high compressive stress area has a gradual transition to a relatively lower compressive stress.

In consideration of the quantitative analysis of the magnitude of the stress field, the Figure 19 shows the variations

of the three stress components on a circle with a radius of 0.05 mm around the crack tip. As can be observed from the figure, the variation of the closure amount has no influence on the angles corresponding to the peak values of the stress components. For the stress components σ_x and τ_{xy}, the absolute values of the extreme values decrease significantly with the increase of closure amount, and the corresponding reductions in the magnitude for σ_x and τ_{xy} when the closure amount changes from 0 to 1 are about 22.7% to 40.5% and 0% to 28.9%, respectively. For the stress component σ_y, the increase of the closure amount makes the absolute value of the maximum value decrease and the absolute value of the minimum value increases by 79.6% and 14.9%, respectively.

(a)

(b)

(c)
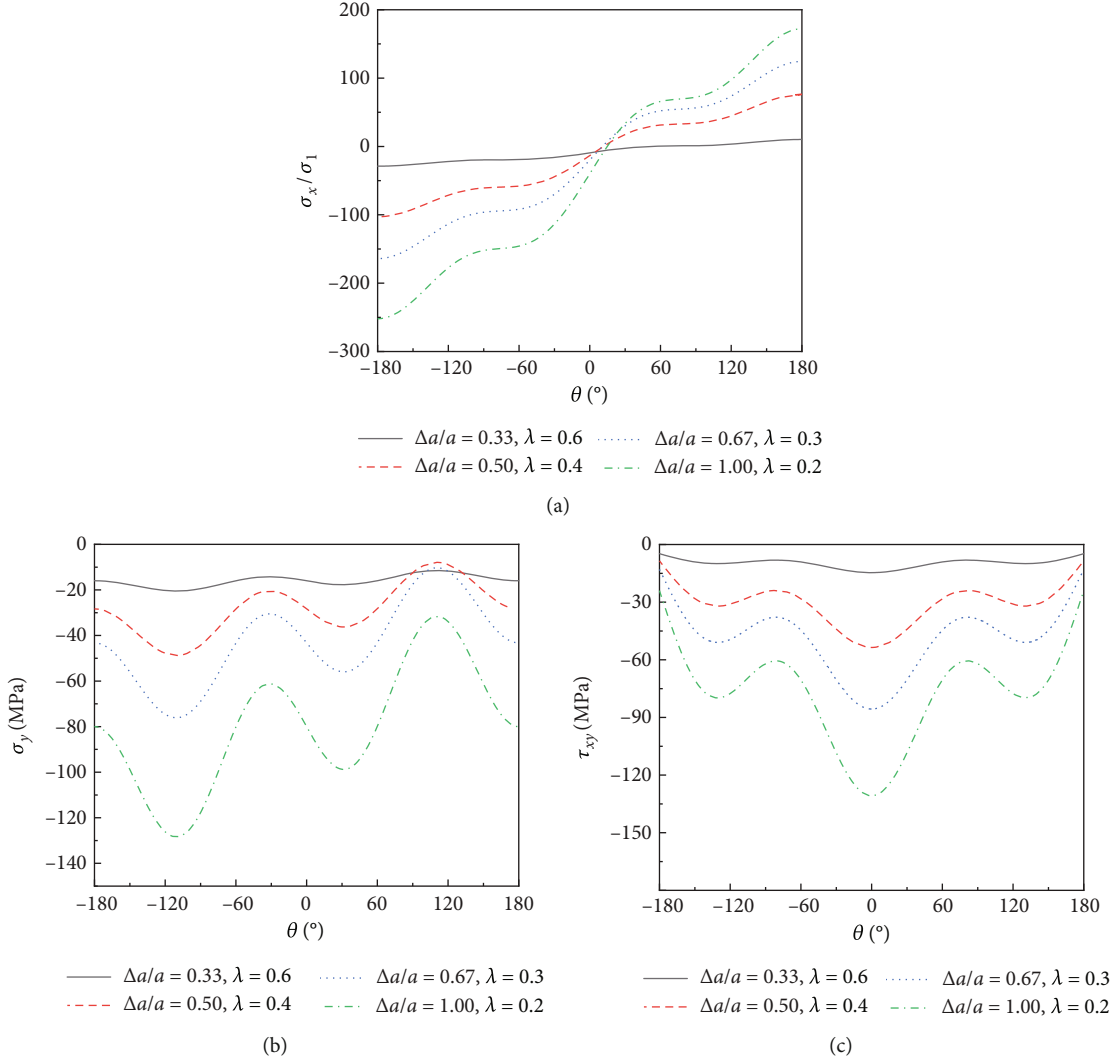
Figure 25: Comparison of stress components on a circle with radius of 0.05 mm around the crack tip at different closures and confining pressure coefficients: (a) σ_x; (b) σ_y; and (c) τ_{xy}.

5.2. The Influence of Closure Amount under Variable Stress.
Besides under constant stress, this section will deal with the influence of closure amount on the evolution of the stress field under variable stress. Considering the conventional loading path shown in Figure 20, the confining pressure coefficient $\lambda = 1$ in the initial state and gradually decreases for a gradually applied stress σ_1. Due to the existence of the confining pressure, the coefficient is close to 0, but not 0.

It is assumed that the closure amount varies linearly with the increase of vertical stress, that is

$$\Delta a/a = \sigma_1/\sigma_1^{\max}, \qquad (68)$$

where the $\sigma_1^{\max}$ is the maximum vertical stress applied during loading. Let $\sigma_3 = 20$ MPa and $\sigma_1^{\max} = 100$ MPa; thus, the closure amount is 0.2 at the initial state of loading and gradually becomes larger and tends to be 1 as gradually applied stress σ_1. Combining the confining pressure coefficient, it can be summarized that the confining pressure coefficient λ gradually decreases while the closure amount $\Delta a/a$ gradually increases as the loading proceeds.

The Equations (8) and (9) illustrate that the relative sliding of the crack surfaces in the closed region requires a particular condition. Consequently, Figure 21 shows the relationship between the stress intensity factor K_{II} and confining pressure coefficient λ. As can been seen from the figure, the stress intensity factor $K_{II} \leq 0$ when $0.68 \leq \lambda \leq 1$, indicating that the shear stress on the closed surfaces is less than the frictional resistance, so that no relative sliding of crack surfaces occurs and the stress field model is not applicable. Nevertheless, the stress intensity factor is more than 0 when λ in the range of $0.2 \leq \lambda < 0.68$, and the stress field model is applicable since relative sliding of crack surfaces occurs.

Similarly, a finite domain with a size of 70×70 mm^2 contains a crack with length of 20 mm, and inclination angle of 30° was also selected as the observed area. The distributions of the three stress components around the crack were investigated at the confining pressure coefficients of 0.6,

0.4, 0.3, and 0.2, respectively, and the corresponding vertical stresses were 33.33 MPa, 50 MPa, 66.67 MPa and 100 MPa, respectively, and the corresponding closure amounts were 0.33, 0.50, 0.67, and 1.00, respectively. The variations of the contour plots around the crack of the three stress components σ_x, σ_y, and τ_{xy} during the loading process are shown in Figures 22, 23, and 24, respectively.

The distributions of the three stress components exhibit apparently different characteristics at various confining pressure coefficients, as can be seen from Figures 22–24. For the three stress components, the distribution of their contour plots in the observed area has a uniform character, and slight stress concentration effect occurs at the crack tip. As the loading proceeds, there is stress concentration effect in the area near the tip which is more relatively obvious in magnitude compared to the area far from the tip. For the stress components σ_x and σ_y, the high stress and low stress regions are distributed on both sides of the crack tip, respectively. For a gradually applied stress σ_1, the high stress region gradually transforms into a relatively low stress, while the low stress region gradually transforms into a relatively high stress. Finally, most of the observed area is distributed with low stress. For the stress component τ_{xy}, it is on the both sides of crack surface where the low stress is distributed, but on the two tips where the high stress is distributed. As the loading proceeds, the tendencies of stress both in both sides of crack surface and the area near the tip will preferably decrease. To conclude, it can be considered that the stress around the crack surface and near the tip, whether in the region of high stress or low stress, tends to transform into a lower stress as the loading progresses.

As the closure amount $\Delta a / a$ increases and confining pressure coefficient decreases during the loading progress, the variation of the stress component on a radius of 0.05 mm circle around the crack tip is displayed in Figure 25. At the initial state, the magnitudes of three component stresses changed a little on the circle around the tip due to the large confining pressure coefficient, although closure amount is relatively small. As the loading proceeds, the component stress fluctuates significantly with the angle θ. Specifically, it can be clearly observed that when the closure amount changes from 0.33 to 1 together with the confining pressure coefficient changes from 0.6 to 0.2, the maximum absolute values of the extreme values of the three stress components are 8.7, 6.3, and 9.1 times of the initial state, respectively.

The above analysis sufficiently demonstrates that the closure amount of crack has a significant effect on the evolution of the stress field, and it is necessary to consider the change in closure caused by the boundary stress during the compression loading, which will be certainly helpful to have a better and a more accurate understanding of the fracture behavior of cracks inside of the structure.

6. Conclusions

A prediction model for stress fields around the semiclosed crack in deep-water structures is innovatively developed in this study, where the compressive and frictional effects between crack surfaces, as well as the closure amount in the closed region, are comprehensively considered. The following conclusions can be drawn:

(1) The stress fields around the semiclosed crack under compression are derived based on the boundary conditions, which include both singular terms containing the stress intensity factor K_{II} and nonsingular terms containing the three T-stresses (T_x, T_y, and T_{xy}). These terms are critically related to deep-water pressure, friction coefficient, and closure amount in the closed region. Furthermore, the fact that K_{I} singularity does not exist in the crack tip under compression is proved theoretically

(2) According to comparisons between isochromatic fringe patterns obtained from the experiments and the proposed model herein, predicted results are in excellent agreements with the experimental ones, demonstrating that the proposed model can accurately and reasonably predict the actual stress field of semiclosed crack than the previous models

(3) The closure amount of the crack surfaces is one of the key factors for determining the stress fields around the crack. With the increase of the closure amount, the stress of each component around the crack always tends to change to the lower stress. Under the condition of constant stress, the degree of stress concentration at the tip is negatively correlated with the closure amount. However, under the variable stress, a positive correlation is presented between the closure amount and the degree of stress concentration at the tip

Data Availability

No data were used to support this study

Conflicts of Interest

The authors declare that they have no conflicts of interest.

Acknowledgments

References

[1] M. Abbas and M. Shafiee, "An overview of maintenance management strategies for corroded steel structures in extreme marine environments," *Marine Structures*, vol. 71, article 102718, 2020.

[2] J. Yan, X. Liu, J. Y. R. Liew, X. Qian, and M. Zhang, "Steel-concrete-steel sandwich system in Arctic offshore structure: materials, experiments, and design," *Materials & Design*, vol. 91, pp. 111–121, 2016.

[3] M. Nour Eldin and J. Kim, "Sensitivity analysis on seismic life-cycle cost of a fixed-steel offshore platform structure," *Ocean Engineering*, vol. 121, pp. 323–340, 2016.

[4] M. G. Alexander and G. Nganga, "Types of marine concrete structures," in *Marine Concrete Structures*, M. G. Alexander, Ed., pp. 17–64, Woodhead Publishing, Duxford, UK, 2016.

[5] A. Mathern, C. von der Haar, and S. Marx, "Concrete support structures for offshore wind turbines: current status, challenges, and future trends," *Energies*, vol. 14, no. 7, p. 1995, 2021.

[6] B. P. Hughes and A. T. Mahmood, "Laboratory investigation of early thermal cracking of concrete," *ACI Materials Journal*, vol. 85, no. 3, pp. 164–171, 1988.

[7] I. Maruyama and P. Lura, "Properties of early-age concrete relevant to cracking in massive concrete," *Cement and Concrete Research*, vol. 123, article 105770, 2019.

[8] I. Lotsberg, G. Sigurdsson, A. Fjeldstad, and T. Moan, "Probabilistic methods for planning of inspection for fatigue cracks in offshore structures," *Marine Structures*, vol. 46, pp. 167–192, 2016.

[9] R. Jiang, F. Dai, Y. Liu, A. Li, and P. Feng, "Frequency characteristics of acoustic emissions induced by crack propagation in rock tensile fracture," *Rock Mechanics and Rock Engineering*, vol. 54, no. 4, pp. 2053–2065, 2021.

[10] F. Bencardino, L. Rizzuti, G. Spadea, and R. N. Swamy, "Implications of test methodology on post-cracking and fracture behaviour of steel fibre reinforced concrete," *Composites Part B: Engineering*, vol. 46, pp. 31–38, 2013.

[11] S. B. Tang, "The effect of T-stress on the fracture of brittle rock under compression," *International Journal of Rock Mechanics and Mining Sciences*, vol. 79, pp. 86–98, 2015.

[12] X. Li, G. Liu, and K. Y. Lee, "Effects of T-stresses on fracture initiation for a closed crack in compression with frictional crack faces," *International Journal of Fracture*, vol. 160, no. 1, pp. 19–30, 2009.

[13] M. L. Williams, "On the stress distribution at the base of a stationary crack," *Journal of Applied Mechanics*, vol. 24, no. 1, pp. 109–114, 1957.

[14] M. A. Hussain, S. L. Pu, and J. H. Underwood, *Strain energy release rate for a crack under combined mode I and mode II*, ASTM International, 1974.

[15] R. W. Margevicius, J. Riedle, and P. Gumbsch, "Fracture toughness of polycrystalline tungsten under mode I and mixed mode I/II loading," *Materials Science and Engineering: A*, vol. 270, no. 2, pp. 197–209, 1999.

[16] M. Gupta, R. C. Alderliesten, and R. Benedictus, "A review of T-stress and its effects in fracture mechanics," *Engineering Fracture Mechanics*, vol. 134, pp. 218–241, 2015.

[17] R. M. Andrews and S. J. Garwood, "An analysis of fracture under biaxial loading using the non-singular T-stress," *Fatigue & Fracture of Engineering Materials & Structures*, vol. 24, no. 1, pp. 53–62, 2001.

[18] M. M. Mirsayar, "On fracture of kinked interface cracks - the role of T-stress," *Materials & Design*, vol. 61, pp. 117–123, 2014.

[19] Z. Zhu, L. Wang, B. Mohanty, and C. Huang, "Stress intensity factor for a cracked specimen under compression," *Engineering Fracture Mechanics*, vol. 73, no. 4, pp. 482–489, 2006.

[20] T. Zheng, Z. Zhu, B. Wang, and L. Zeng, "Stress intensity factor for an infinite plane containing three collinear cracks under compression," *ZAMM-Journal of Applied Mathematics and Mechanics/Zeitschrift für Angewandte Mathematik und Mechanik*, vol. 94, no. 10, pp. 853–861, 2014.

[21] X. Fan, H. Yu, Z. Deng, Z. He, and Y. Zhao, "Cracking and deformation of cuboidal sandstone with a single nonpenetrating flaw under uniaxial compression," *Theoretical and Applied Fracture Mechanics*, vol. 119, article 103284, 2022.

[22] K. Zhang, Z. Jiang, X. Liu, K. Zhang, and H. Zhu, "Quantitative characterization of the fracture behavior of sandstone with inclusions: experimental and numerical investigation," *Theoretical and Applied Fracture Mechanics*, vol. 121, article 103429, 2022.

[23] H. Yang, H. Lin, Y. Chen et al., "Influence of wing crack propagation on the failure process and strength of fractured specimens," *Bulletin of Engineering Geology and the Environment*, vol. 81, no. 1, pp. 1–19, 2022.

[24] H. Liu, "Wing-crack initiation angle: a new maximum tangential stress criterion by considering T-stress," *Engineering Fracture Mechanics*, vol. 199, pp. 380–391, 2018.

[25] Y. Fan, Z. Zhu, Y. Zhao, L. Zhou, H. Qiu, and C. Niu, "Analytical solution of $\_T\_$ -stresses for an inclined crack in compression," *International Journal of Rock Mechanics and Mining Sciences*, vol. 138, article 104433, 2021.

[26] M. Feng, X. Zhou, Y. Zhang, and P. Zhou, "Theoretical and experimental study considering the influence of T-stress on the fracture behavior of compression-shear crack," *Advances in Materials Science and Engineering*, vol. 2022, Article ID 2706896, 18 pages, 2022.

[27] N. I. Muskhelishvili, "General solution of the fundamental problems for regions bounded by one contour," in *Some Basic Problems of the Mathematical Theory of Elasticity: Fundamental Equations Plane Theory of Elasticity Torsion and Bending*, N. I. Muskhelishvili, Ed., pp. 317–333, Springer Netherlands, Dordrecht, 1977.

[28] K. B. Broberg, *Cracks and Fracture*, Academic Press, London, 1999.

[29] K. Khan and N. A. Al-Shayea, "Effect of specimen geometry and testing method on mixed mode I–II fracture toughness of a limestone rock from Saudi Arabia," *Rock Mechanics and Rock Engineering*, vol. 33, no. 3, pp. 179–206, 2000.

[30] H. Liu and S. Lv, "A model for the wing crack initiation and propagation of the inclined crack under uniaxial compression," *International Journal of Rock Mechanics and Mining Sciences*, vol. 123, article 104121, 2019.

[31] P. Isaksson and P. Ståhle, "Prediction of shear crack growth direction under compressive loading and plane strain conditions," *International Journal of Fracture*, vol. 113, no. 2, pp. 175–194, 2002.

[32] J. G. Williams and P. D. Ewing, "Fracture under complex stress-the angled crack problem," *International Journal of Fracture Mechanics*, vol. 8, no. 4, pp. 441–446, 1972.

[33] B. Košťák and J. Kozák, "Photoelastic analysis of a Seismoactive crack," in *Optical Methods in Dynamics of Fluids and Solids. International Union of Theoretical and Applied Mechanics*, M. Píchal, Ed., Springer, Berlin, Heidelberg, 1985.

[34] S. Lee and G. Ravichandran, "An investigation of cracking in brittle solids under dynamic compression using photoelasticity," *Optics and Lasers in Engineering*, vol. 40, no. 4, pp. 341–352, 2003.

[35] L. V. Stepanova and V. S. Dolgikh, "Interference-optical methods in mechanics for the multi-parameter description of the stress fields in the vicinity of the crack tip," *Journal of Physics: Conference Series*, vol. 1096, article 12117, 2018.

[36] E. Hoek and Z. T. Bieniawski, "Brittle fracture propagation in rock under compression," *International Journal of Fracture Mechanics*, vol. 26, no. 4, pp. 276–294, 1984.

[37] S. Lee and G. Ravichandran, "Crack initiation in brittle solids under multiaxial compression," *Engineering Fracture Mechanics*, vol. 70, no. 13, pp. 1645–1658, 2003.

[38] M. Wang, Z. M. Zhu, and J. H. Liu, "The photoelastic analysis of stress intensity factor for cracks around a tunnel," *Applied Mechanics and Materials*, vol. 142, pp. 197–200, 2012.